ACS APPLIED MATERIALS & INTERFACES

Energy, Environmental, and Catalysis Applications

Marimo Bead-Supported Core-Shell Nanocomposites of Titanium Nitride and Chromium-Doped Titanium Dioxide as Highly Efficient Water Floatable Green Photocatalyst

Manpreet Kaur, Satish Laxman Shinde, Satoshi Ishii, Min-Wen Yu, Wipakorn Jevasuwan, Naoki Fukata, Yunxiang Li, Jinhua Ye, and Tadaaki Nagao

ACS Appl. Mater. Interfaces, **Just Accepted Manuscript** • Publication Date (Web): 29 May 2020

is published by the American Chemical Society. 1155 Sixteenth Street N.W., Washington, DC 20036

Marimo Bead-Supported Core-Shell Nanocomposites of Titanium Nitride and Chromium-Doped Titanium Dioxide as Highly Efficient Water Floatable Green Photocatalyst

Manpreet Kaur[1,4,†], Satish Laxman Shinde[1,†], Satoshi Ishii[1,2*], Min-Wen Yu[1,3], Wipakorn Jevasuwan[1], Naoki Fukata[1,2], Yunxiang Li[1], Jinhua Ye[1], and Tadaaki Nagao[1,4*]*

[1]International Center for Materials Nanoarchitectonics (WPI-MANA), National Institute for Materials Science (NIMS), Tsukuba, Ibaraki, 305-0044, Japan

[2]Faculty of Pure and Applied Sciences, University of Tsukuba, Tsukuba, Ibaraki 305-8577, Japan

[3]Institute of Lighting and Energy Photonics, College of Photonics, National Chiao Tung University, Tainan 71150, Taiwan

[4]Department of Condensed Matter Physics, Hokkaido University, Sapporo, Hokkaido, 060-0810, Japan

KEYWORDS. Photocatalysis, titanium dioxide, titanium nitride, core-shell, alginate.

ABSTRACT The release of industrial untreated wastewater creates a hazardous impact on the environment. In this regard, the development of environment friendly catalyst is of paramount importance. Here, we report a highly efficient and reusable core-shell TiN/SiO_2/Cr-TiO_2 (TSCT) photocatalyst which is composed of SiO_2-cladded titanium nitride (TiN) nanoparticles (NPs) decorated with Cr-doped TiO_2 NPs for the removal of organic contaminant from water. The TiN NPs serve as the main light absorber component with excellent visible light absorption along with Cr-TiO_2 NPs. The TSCT shows remarkable improvement in the photodecomposition of methylene blue (MB) over Cr-TiO_2 and TiO_2 NPs. An efficient structural design is proposed by adopting calcium alginate beads (P-Marimo beads) as transparent scaffold for supporting our TSCT which exhibits floatable nature on the water surface and realizes easy handling as well as excellent reusability for multipurpose water purification. Surprisingly, our TSCT is found to keep its catalytic activity even after the

illumination is turned off. Our proposed P-Marimo-encapsulated TSCT can be utilized as an excellent green photocatalyst with high photocatalytic performance, recyclability and easy handling.

1. INTRODUCTION

Currently, solar energy driven green nanotechnology is attracting great interest in many countries to solve environmental hazards due to the release of toxic dyes, pesticides, volatile organic compounds, harmful gases, and bacteria in different media [1-3]. Serious efforts have been devoted to develop hybrid nanomaterials for environmental clean-up, water purification, antimicrobial activity etc [4-6]. The organic contaminants can either be oxidized/reduced directly by the photocatalysts or be eliminated by locally generated reactive oxygen species (ROS) including the superoxide radical $O_2^{-\bullet}$, hydroxyl radical ($^{\bullet}OH$), and peroxide (H_2O_2) [7-8]. In this context, TiO_2 has been proved to be a material for the decontamination of industrial wastewater [9]. However, TiO_2 has a large band gap (~3.2 eV), which means that it is inactive under visible irradiation. There have been several attempts to improve the catalytic activity of TiO_2. One of the simplest method is to synthesize the mixtures of anatase and rutile phases of TiO_2 which has higher photocatalytic activity than those of the single phases [10-11]. To increase the visible light activity of TiO_2, doping of TiO_2 is a quite effective approach [12]. Among transition metal ions, Cr^{3+} ions exhibit an isomorphic replacement of Ti^{4+} ions in TiO_2 crystal lattice and enables TiO_2 to absorb both ultraviolet (UV) and visible light [13-14]. Yet, the absorption capability of Cr-TiO_2 in visible region still needs further improvement.

Aiming at enhancing visible light activity, incorporating plasmonic materials to photocatalysts has recently come into focus [15-16]. The surface plasmon resonance of silver (Ag) and gold (Au) nanoparticles (NPs) incorporated with TiO_2 has been investigated for the enhancement of photo reactivity under the irradiation of UV and a broad range of visible light [17-18]. However, expensive noble metals are incompatible with large scale industrial applications. These drawbacks were the driving force for investigating alternative plasmonic materials for photocatalysis applications. Among alternative plasmonic materials, titanium nitride (TiN) is one of the promising candidates. TiN is chemically stable, inexpensive, and has inherently broad plasmon resonance covering the entire solar spectrum from the visible to the near infrared (NIR) region. When TiN NPs are attached to a semiconducting photocatalysts, photo-excited carriers in the TiN can be injected into the semiconductor [19], thus enhancing the photocatalytic activity. TiN has been successfully used to enhance the photocatalytic activities

of TiO_2 [20-21]. It is important to note that TiN NPs can also improve the photocatalytic activity of photocatalyst by improving the conductivity of the photocatalytic composites [22]. Separation of both effects and the possibility of synergistic enhance of photocatalytic activities are yet to be explored [23].

Here, we report a highly efficient and environmentally compatible photocatalyst consist of core-shell nanostructure of chromium-doped TiO_2 (Cr-TiO_2) NPs and SiO_2 cladded TiN NPs (SiO_2/TiN). The TiN/SiO_2/Cr-TiO_2 (TSCT) nanostructure catalyst showed enhanced light absorption and rapid separation of photogenerated electron–hole pairs as well as greater specific surface area compared with Cr-TiO_2 NPs. Ultrathin ~2 nm SiO_2 cladding layer to the TiN NPs was the key for better chemical stability and higher heat resistance. We also adopted a novel scheme to make this photocatalyst easy to handle and recycle [24-25]. We fabricated hybrid structure by fixing TSCT into alginate network that has high solar transparency as well as water permeability. This TSCT embedded alginate constituted 3D photocatalytic beads which imitated the natural *"Marimo algae (Aegagropila linnaei),"* a rare growth form of a filamentous green algae. We named this 3D photocatalytic balls as, *"P-Marimo"* (Figure 1) and experimentally demonstrated its high photocatalytic activity together with its excellent recyclability and its long lifetime.

The obtained photocatalytic activities of the synthesized photocatalysts were in the order as TSCT > Cr-TiO_2 >TiO_2 under solar light irradiation. The 99% decomposition of 10 μM MB was achieved within 10 and 15 minutes by TSCT and P-Marimo, respectively. Surprisingly, after the light irradiation for short duration on TSCT/dye solution, it kept its catalytic activity, *even in the dark*, to decompose organic dyes due to its ability of superoxides species generation. Reaction mechanism was investigated to explain the observed phenomenon. The low-cost, long-life, and environmentally friendly nature of our *P-Marimo*-supported photocatalysts will open a promising route for solar water purification.

2. EXPERIMENTAL SECTION

Synthesis steps:

Chemicals: Sodium alginate used in our study was a commercial product of KIMICA Corporation. Titanium (*IV*) butoxide, $Ti[O(CH_2)_3CH_3]_4$, chromium (III) nitrate nonahydrate, $Cr(NO_3)_3.9H_2O$ and methylene blue (MB) were supplied from FUJIFILM Wako Pure Chemical Corporation. MB dye solution was prepared using deionized water from a Milli-Q

purification unit. Titanium nitride NPs were purchased from Nisshin Engineering Inc, whose size was around 40 nm [26].

Synthesis: To study the catalytic performance of TiN decorated with Cr-TiO_2 and to compare with the combination of TiN with different phases of TiO_2, various photocatalysts were synthesized.

Synthesis of conventional TiO_2: To obtain the TiO_2 NPs, in the first step, the 2 ml of titanium(IV) butoxide ($Ti[O(CH_2)_3CH_3]_4$) was slowly dropped into 5 ml ethanol and vigorously stirred for 1 hour at room temperature (RT). In the second step, the mixture of 240 µl water, 5 ml ethanol and 260 µl HNO_3 was added dropwise to the initial solution under vigorous stirring. The resultant solution was stirred for an additional 60 minutes at room temperature to increase its homogeneity; this further baked at 78 °C for 2 hours under vacuum condition. The obtained powder was further thermally treated in ambient air at 400 °C for 4 hours. The heating rate was 1 °C/min to reach 400 °C. The obtained sample was used as it was for further characterizations.

Synthesis of visible-active Cr-TiO_2: The mixture of 5 ml ethanol and 0.120 g chromium (III) nitrate ($Cr(NO_3)_3$) was vigorously stirred for 1 hour at RT and 2 ml of $Ti[O(CH_2)_3CH_3]_4$ was added dropwise into the solution. A green solution was obtained. Further, the mixture of 240 µl water, 5 ml ethanol and 260 µl HNO_3 was added dropwise in the solution. The Cr-TiO_2 powder was obtained after thermal treatment of the solution by following the similar steps as mentioned for the TiO_2 synthesis.

Synthesis of biphasic Cr-TiO_2 (B-Cr-TiO_2): Initially adding the 1 weight (wt)% TiN NPs solution in 5 ml ethanol and following the similar procedure used for synthesizing Cr-TiO_2, the biphasic-Cr-TiO_2 (B-Cr-TiO_2) powder was obtained. After the thermal treatment, the black color of TiN disappeared and the synthesized materials showed pale yellow color, indicating the metallic TiN NPs were lost and B-Cr-TiO_2 was absorbing blue light component. The Figure S1 show the optical camera images of different samples.

Synthesis of heat-resistive TiN NPs (SiO_2/TiN NPs): To fabricate a very thin SiO_2 protection layer on TiN NPs, 500 µl of 5.0 mM 3- aminopropyltriethoxysilane (APTES) aqueous solution was added in 5 ml water and stirred for 30 minutes. Then, 0.54 wt% sodium silicate aqueous solution was added, and the obtained solution stirred for five minutes at 100 °C. Afterwards, 1 wt% TiN NPs powder was added and kept the solution on stirring for 1 hour at 80 °C as shown

in the supporting information Figure S2. The resultant sample was centrifuged and collected from the un-reactant ions and re-dispersed into 5 ml ethanol for further use.

Synthesis of TiN/SiO_2/Cr-TiO_2 (TSCT): Using SiO_2 cladded TiN NPs and following the similar procedure used for synthesizing the B-Cr-TiO_2, the dark brown colored powder of TSCT core-shell structure was obtained. The TiN/SiO_2 to Cr-TiO_2 weight ratio was 1:2 in TSCT sample. The SiO_2 formed a conformal shell on the TiN NPs. Also, by varying the TiN/SiO_2 to Cr-TiO_2 ratio, TSCT core-shell structure containing 0.5 and 2 wt% SiO_2/TiN NPs was fabricated. For the characterizations and catalytic measurements 1 wt% TiN/SiO_2 in TSCT core-shell structure was used, otherwise specified. The TSCT NPs size can be tuned by varying the TiN NPs size and concentration of precursor, reaction time and temperature during sol-gel preparation of Cr-TiO_2.

Synthesis of recyclable 3D photocatalytic alginate balls (P-Marimo): 2 mg/ml of photocatalyst (TSCT) powder and 2 wt% of sodium alginate aqueous solution were stirred overnight. This solution was dropwise added in 1 wt% $CaCl_2$ (50 µl), using a micropipette to obtain the TSCT embedded Ca–alginate beads (2-3 mm average diameter). The P-Marimo were kept in the $CaCl_2$ solution at RT for 2 hours. The P-Marimo catalysts were washed with pure water and used for dye degradation and after catalytic reactions again washed with pure water and stored in 1 wt% $CaCl_2$ for reuse. Using the similar procedure, P-Marimo of TiO_2 and Cr-TiO_2 were fabricated.

Catalytic reactions: The catalytic experiments were performed for different concentrations (5-15 µM) of the dyes with different loadings (1−3 mg/ml) of photocatalyst. The catalysis experiments were carried out in 50 mL cylindrical pyrex vessel in dark and light environment. For all the experiments of dye degradation, the 20 µl H_2O_2 were added in the dye solution which produced $^{\bullet}OH$ radicals initially [7, 27]. The magnetic stirrer was used for stirring the solutions. The stirring speed was kept constant at 500 rpm for all the experiments. A solar simulator (XES-40S1, San-Ei Electric) at 100 mW cm^{-2} irradiance was used as an artificial sunlight source. After stirring the solution of reaction vessels in a dark box for 5 min, the vessels were irradiated with the solar simulator for different time interval and the degraded dye solution was then transferred to UV-Quartz cuvette to measure the dye degradation using a UV-Visible spectrophotometer (V-570, JASCO). The absorbance spectra were measured by taking out 2 ml solution with discrete time interval. The NPs were removed by centrifugation at 10000 rpm for 5 min before absorbance measurement whereas in the case of P-Marimo,

water was separated directly without any further separation step. For the reusability test, the catalyst was allowed to settle for 30 min, separated and rinsed with deionized water for several times and used for next cycles. For the detection of radical scavenger effect, 2 mg/mL of catalyst in 10 μM MB in the various solvents such as methanol (99.8%), N_2 purged (2 h) H_2O, 5 mM $AgNO_3$ and 5 mM Na_2-EDTA were used. For the detection of $^{\bullet}OH$ radicals, 2 mg/mL of catalyst suspended in aqueous solution of 0.5 mM terephthalic acid (TA) in 2 mM NaOH was used and stirred. In a regular time interval, 1 mL solution was taken out and the photoluminescence (PL) spectrum was recorded at an excitation wavelength of 315 nm.

The apparent quantum yield (AQY) measurement was performed as follows: A 300W Xe arc lamp equipped with glass filters consisting of band-pass and cut off filters to control the 440 nm wavelength regions of the incident light was used. A 50 mg of as-prepared catalyst was spread firmly on a plate (area, 2.2 cm^2). Then the isopropanol (IPA) (ca. 1000 μmol) was injected into the vessel and a gas chromatograph and flame ionization detector was used to detect the concentrations of IPA and acetone.

Characterization:

The morphology of the catalyst powder was studied by an SEM (Hitachi FE-SEM SU8230). XRD measurements were taken by a Rigaku Ultima III, Rint 2000. TEM images and XPS spectra were recorded by the JEOL JEM 2100F instrument, and Micro-XPS (Quantera SXM) instrument having the resolution of ~0.5 eV, respectively. Raman spectra were obtained by a WITec microscope 300 alpha with a 532 nm Nd:YAG diode laser. Brunauer–Emmett–Teller (BET) surface area was measured by Quantachrome, Autosorb-iQ. The PL measurements were carried out by JASCO, FP8500 fluorescence spectrometer. The micro PL spectroscopy (excitation wavelength 325 nm) were employed to check the optical properties. Diffuse reflection spectra of the samples were recorded with a UV-VIS spectrometer equipped with an integrating sphere. To measure the paramagnetic species, the electron paramagnetic resonance (EPR) spectrometer (Bruker, Rheinstetten, Germany) was set to a center field of 3520 G, a sweep width of 100 G, a microwave frequency of 9.876 GHz, a modulation frequency of 100 kHz, and power of 6.37 W.

3. RESULTS AND DISCUSSION

Figure 1 shows a scheme of the TSCT immobilization method in Ca–alginate beads. The sodium alginate in water has sodium ions and alginate. After adding the sodium alginate

aqueous solution in the $CaCl_2$, the calcium ions functioned as connecting bridges (gel matrix) between the alginate chains and immobilizes the TSCT in between them, forming porous P-Marimo structure. The porous structure of P-Marimo provides excellent permeability for water molecules to freely move inside the P-Marimo. Figure S3 shows the SEM images of the as prepared TiO_2, Cr-TiO_2, TSCT and TiN NPs. The TiO_2, Cr-TiO_2 and TSCT NPs have approximately spherical shapes having average particle size of ~40 nm, ~40 nm, and ~80 nm, respectively. The SEM image of TiN NPs shows their cubic structure having average particle size of ~40 nm.

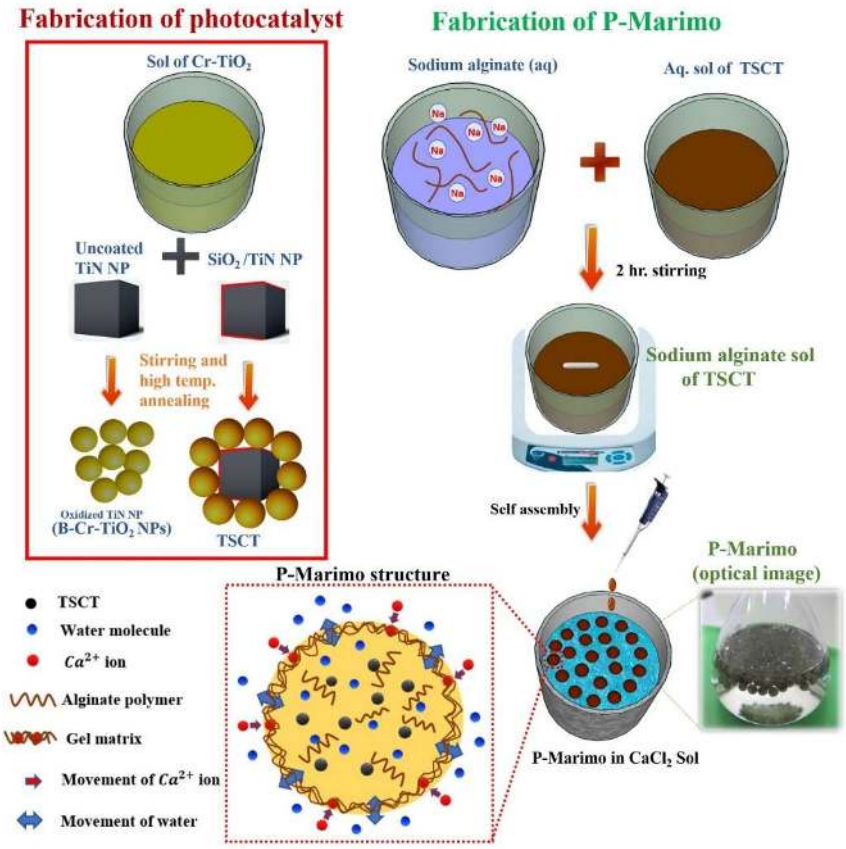

Figure 1. Schematic representation of TiN/SiO_2/Cr-TiO_2 (TSCT) and B-Cr-TiO_2 nanostructure fabrication using with and without SiO_2 cladded TiN NPs, respectively. Fabrication of TSCT P-Marimo structure is also shown.

The XRD patterns of TiO_2, Cr-TiO_2, and TSCT are shown in Figure 2a. As synthesized TiO_2 shows strong peaks of anatase phase, while Cr-TiO_2 show broad peaks of anatase phase due to the Cr doping [28]. The TSCT sample containing 1wt% SiO_2/TiN NPs exhibit strong and broad

peaks of both cubic phase TiN and anatase phase Cr-TiO_2, this confirm the formation of Cr-TiO_2 decorated TiN NPs.

However, when bare TiN NPs (i.e. without coating thin SiO_2 layer to form core-shell structure of TiN/Cr-TiO_2) were used, the TiN NPs oxidized during high temperature annealing to anatase and rutile phases of TiO_2, and forms a mixed phase, or biphasic Cr-TiO_2 (B-Cr-TiO_2), this was confirmed from XRD pattern (Figure S4) and illustrated in Figure 1 (fabrication of photocatalyst). This indicate that to form TSCT, the thin SiO_2 layer on TiN NPs is required. Further, the XRD pattern of varying SiO_2/TiN NPs concentration i.e. 0.5 to 2 wt% in the TSCT hybrid structure is shown in Figure S5. It is observed that the sample containing 0.5 wt% SiO_2/TiN NPs shows strong peaks of Cr-TiO_2 and very weak peaks of TiN NPs. The sample containing 2 wt% SiO_2/TiN shows strong peaks corresponding to TiN whereas Cr-TiO_2 signal were suppressed. As the amount of TiN NPs increase, the TiN peaks become dominant and Cr-TiO_2 peaks start to suppress. The peaks are indexed to the cubic phase of TiN (JCPDS no. 06-4909) and rutile and anatase phase of TiO_2 (JCPDS no. 21-1276 and 21-1272). The TiN NPs (size ~40 nm) used in this study have cubic phase crystalline structure (Figure S5).

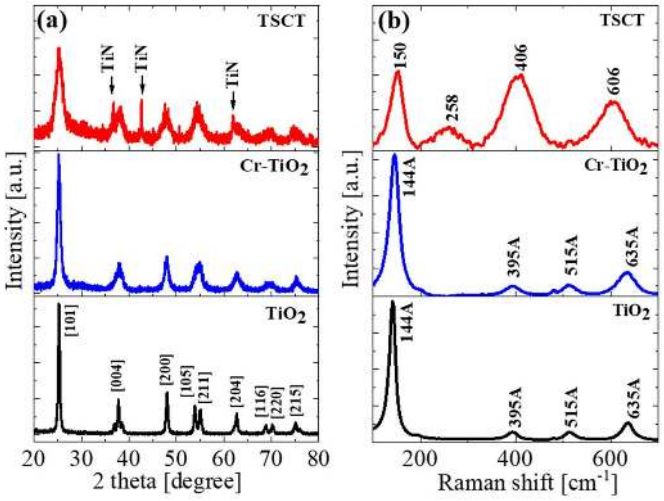

Figure 2. (a) X-ray diffraction patterns (b) Raman spectra of TSCT (containing 1wt% SiO_2/TiN NPs), Cr-TiO_2, and TiO_2 samples. Here, "A" stands for anatase phase.

The Raman spectra of the as synthesized samples are shown in Figure 2b. The TiO_2 and Cr-TiO_2 sample show Raman peaks which correspond to the A1g mode (515 cm^{-1}), B1g modes (395 cm^{-1}, 515 cm^{-1}) and strong Eg modes (144 cm^{-1}, 635 cm^{-1}), confirming the formation of the anatase phase TiO_2 [29-30]. The vibrational mode peak exhibits significant shift as well as asymmetrical broadening associated with phonon confinement effect in the case of TSCT core-

shell structure, which further confirms the presence of TiN and Cr-TiO_2. Raman peaks are very sensitive to the local environment and substitutional doping can significantly influenced the phonon vibrations. Therefore, the Cr-TiO_2 shows broad Raman peaks compared to the TiO_2 due to the substitutional doping of Ti^{4+} with Cr^{3+} [31-33]. The Raman spectra of TiN NPs (Figure S6) shows the characteristic peaks at 235 cm^{-1}, 439 cm^{-1} and 607 cm^{-1} which can be assigned to acoustic and optical modes of TiN [34]. The Raman peaks of TiN at 235 cm^{-1} and 439 cm^{-1} shift to 258 cm^{-1} and 406 cm^{-1} for TSCT, respectively. In Raman spectrum of TiN, the bands below 300 cm^{-1} are associated to the Ti-vibrating modes and the band around 550 cm^{-1} is due to the nitrogen associated optical modes [35].Note that the intensity increase and blueshift in titanium-vibrating modes indicates the increase in nitrogen vacancies, and the existence of nitrogen-vibrating modes indicates titanium vacancies. Also, the grain size effects can produce substantial shifting and broadening of the Raman spectrum. Overall, the variations in the peak positions and intensity of TSCT compared to TiN peaks are associated with the variations in Ti or N vacancies concentrations arisen in the annealing process of synthesizing TSCT. The B-Cr-TiO_2 sample exhibits the vibrational mode of rutile phase at 445 cm^{-1} and 613 cm^{-1} [36], along with anatase phase vibrational modes as shown in Figure S6, which confirmed the mixed phase of B-Cr-TiO_2.

The nitrogen adsorption isotherms of TSCT, TiO_2, TiN, Cr-TiO_2 and B-Cr-TiO_2 samples are shown in Figure S7. The specific surface area values are tabulated in Table S1 along with the crystallite size which was calculated using the Debye–Scherrer formula from XRD peaks (explained in Note S1). As can be seen, the specific surface area decreases from 104.778 m^2/g (for the sample TiO_2) to 70.624 m^2/g (for the sample Cr-TiO_2) and 75.829 m^2/g (for the sample B-Cr-TiO_2). The aggregation formed after the Cr doping in the TiO_2 could reduce the specific surface area than the undoped discrete TiO_2 NPs. Due to the TiN core, the obtained specific surface area of TSCT (149.3 m^2/g) is almost twice as compared to Cr-TiO_2 and B-Cr-TiO_2. A progressive increase in specific surface area of TSCT can be helpful to improve the surface reaction of the NPs and dye loading in comparison with other NPs. The uncovered TiN has larger surface area (206.89 m^2/g) as compared with TSCT, which may result from the smaller crystal size.

The TEM image of the TiN NPs (Figure 3a) shows cubic structures having the average size of ~40 nm, as also confirmed by the SEM image (Figure S3d). The TEM image of TSCT (Figure 3b) shows the cubic TiN NPs as a core cladded with thin SiO_2 and Cr-TiO_2 shell layers. It is observed from the HRTEM image that TiN NPs have very thin SiO_2 (~2 nm) capping layers

which covered the TiN NPs uniformly and Cr-TiO_2 NPs were successfully coated on SiO_2/TiN NPs (Figure 3c). In the HRTEM image of TSCT (Figure 3d), from the inter-planer spacing the TiN NP, SiO_2 and Cr-TiO_2 are clearly distinguishable. The lattice spacing of 0.349 ± 0.05 nm is ascribed to the (101) plane of anatase TiO_2 [37]. In the TEM, the selected area electron diffraction (SAED) and HRTEM images of the Cr-TiO_2 were also taken as shown in Figure S8. The results indicate an inter-planar spacing of 0.351 ± 0.03 nm, which is similar to the Cr-TiO_2 of TSCT. The TEM image of B-Cr-TiO_2 is shown in Figure S9a and from HRTEM image (Figure S9b), the inter-planar spacing is observed to be 0.351 ± 0.03 nm and 0.371 ± 0.03 nm corresponding to anatase and rutile phases of TiO_2 [37]. The SAED shows the diffraction rings corresponding to anatase and rutile phase in inset of Figure S9a.

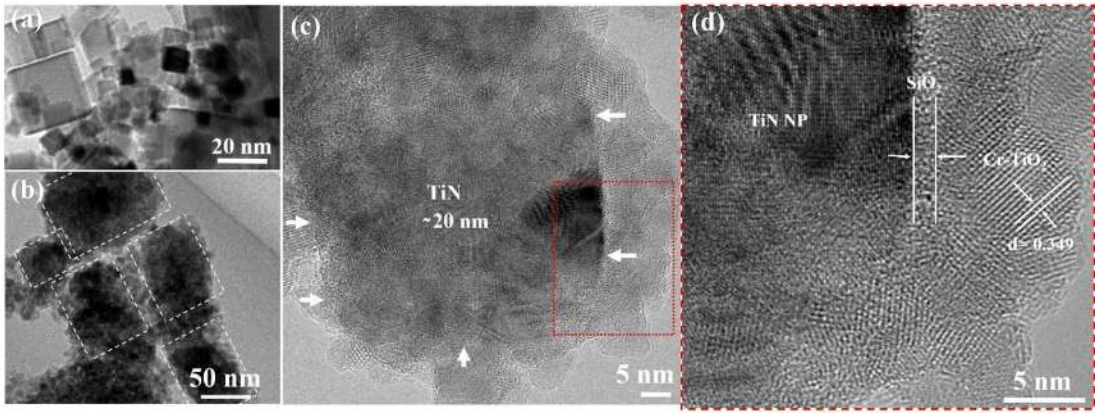

Figure 3. TEM images of (a) TiN NPs and (b) TSCT, where white boxes show TiN NPs covered with Cr-TiO_2 NPs. (c) HRTEM image of TSCT and (d) enlarged view of (c).

The TEM/EDX was also used to investigate the composition of core-shell TSCT sample. The EDX mapping confirm the presence of TiN, SiO_2, Cr and TiO_2 (Figure 4) and the EDX spectrum in Figure 4b, indicates the peaks of N, O, Cr, Ti and Si. Further, the magnified EDX spectrum distinguishes the nitrogen peak from carbon (Figure 4c). Note that carbon peak appears due to the supporting carbon-coated copper grid. Also, the particle size distribution of TiO_2, Cr-TiO_2, TiN and TSCT obtained from the TEM images are shown in Figure S10. The average particle size of the TiO_2, Cr-TiO_2, TiN and TSCT are nearly 6 nm, 15 nm, 30 nm and 70 nm, respectively, which are slightly smaller than the average particle size measured from SEM images (Figure S3). This difference is because, for the TEM measurements the samples were dispersed in water for the sonication and only the smaller particles suspended in water were used for the observation. During the synthesis of TSCT, the Cr-TiO_2 and TiN NPs

aggregated, and the particle size varies from 50 nm to 70 nm as seen in the TEM images (Figure S10d).

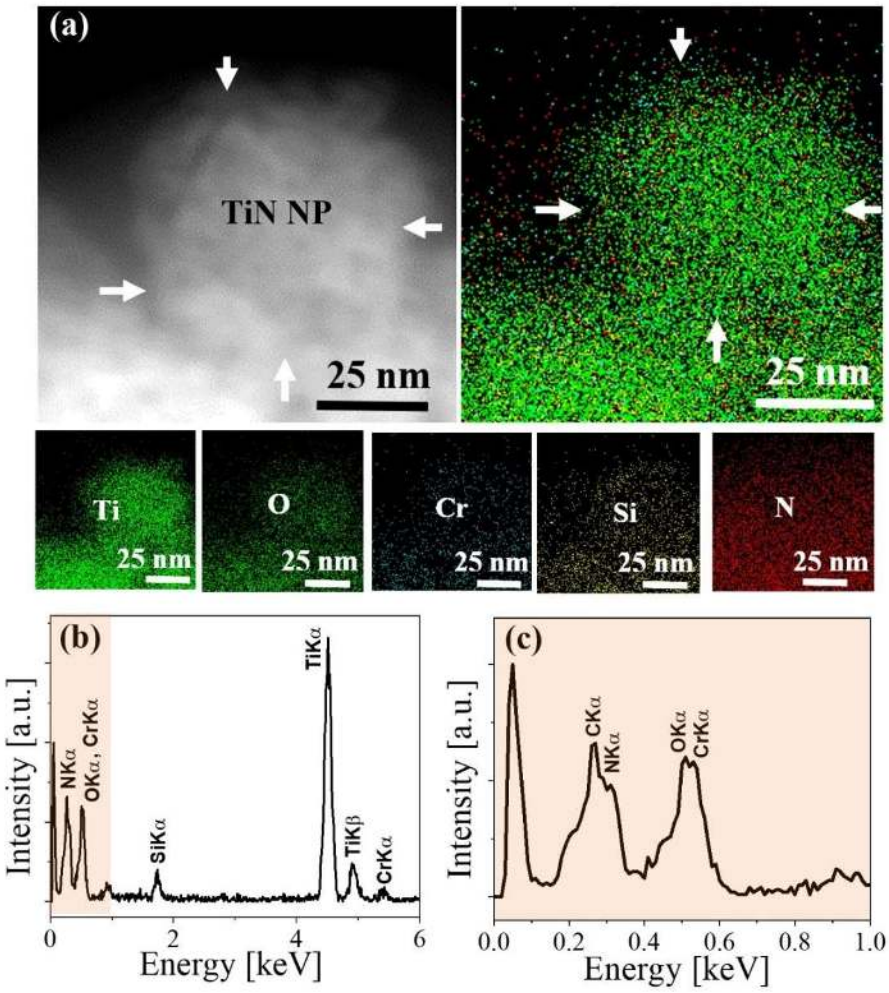

Figure 4. (a) EDX mapping of TSCT, showing the bright-field image, elemental mapping of Ti, O, Cr, Si, N and combined images (white arrow depicts the TiN NP covered with Cr-TiO_2). (b) EDX spectrum of TSCT. (c) Magnified EDX spectrum of the colored area in sub-panel (b).

Additionally, the XPS measurement was performed to investigate the energy states and elemental composition of TSCT sample. High-resolution XPS spectra of Ti 2p, O 1s, Cr 2p and Si 2p are shown in supporting information (Figure S11). In Figure S11a, the binding energy of Ti $2p_3$ peaks is determined to be 458.6 eV which matches with the literature values for crystalline TiO_2 [38]. For O 1s, the major peak at 530.1 eV (Figure S11b) is due to the formation of TiO_2 [38], and the peaks corresponding to 577.2 and 587.0 eV were assigned to the $2p_3$ and $2p_1$ core levels of Cr (Figure S11c) [39]. The spectrum of Si 2p shown in Figure S11d confirms the valence states of Si at 102.7 eV [40], for SiO_2/TiN NPs. Unfortunately, information of the

TiN core inside the TiO_2 shell was not acquired due to the limited probing depth of XPS upto 10 nm.

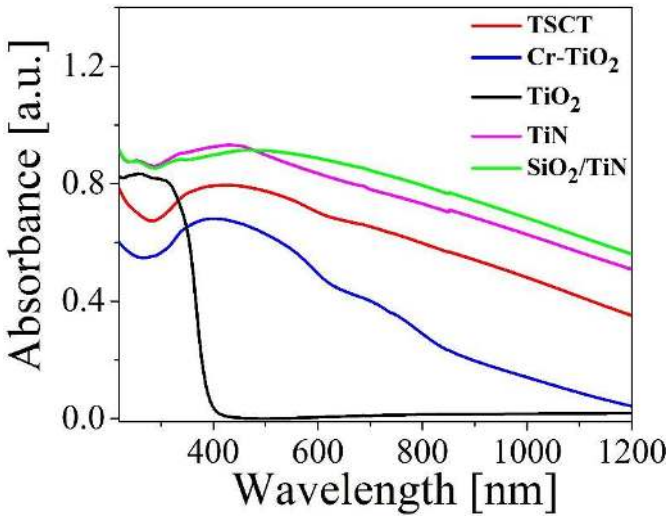

Figure 5. Absorbance spectra of TSCT, Cr-TiO_2, TiO_2, uncoated TiN and SiO_2/TiN NPs.

Absorbance spectra obtained from the reflectance of TSCT, Cr-TiO_2 and TiO_2 along with uncoated TiN and SiO_2/TiN are shown in Figure 5. As TiO_2 is a wide band gap material (band gap ~3.2 eV), it shows strong absorbance in the UV region, while after Cr doping the absorbance is extended to visible region. Absorbance spectra of the uncoated TiN NPs and SiO_2/TiN NPs show broad peak in visible to NIR region. The SiO_2/TiN NPs shows a minor red shift in the absorbance band toward the higher wavelength region, as compared to the uncoated TiN NPs. This minor shift can be attributed to the peak shift in the localized surface plamon resonances induced by the refractive index increase of the surrounding [41]. The absorbance spectrum of TSCT becomes higher compared to that of Cr-TiO_2 but lower than those TiN NPs. The reason is attributed to increased scattering by forming Cr-TiO_2 shells on the TiN NPs.

The electron paramagnetic resonance (EPR) spectroscopy was used for detecting trapped charge carriers or paramagnetic species present in the samples. We have used fully dehydrated TSCT, Cr-TiO_2 and TiO_2 NPs to obtain the EPR spectra for evidencing paramagnetic species and trapping at room temperature where the spectra are as shown in Figure 6. The TiO_2 and Cr-TiO_2 show O^- anion signals constituting g value (spin-Hamiltonian parameter) of 2.009 and 2.008, respectively, which are the most prominent electron signal of paramagnetic materials containing "F-centers" or oxygen vacancies [42-43].

In contrast, a very intense EPR signals at g value of 2.003 was detected in the spectra of TSCT, which confirms the high number of trapped electrons at the surface [44]. These trapped electrons could reduce Ti^{4+} and lead to the generation of Ti^{3+} paramagnetic species according to the following equation,

$$e^- + Ti^{4+} \rightleftharpoons Ti^{3+}$$

$$Ti^{3+} + O_2 \rightarrow Ti^{4+} + O_2{\bullet^-}$$

which has been extensively reported [55], and on the other hand it could reduce surface absorbed O_2 on TSCT active sites, to form superoxide ions. Since TSCT was synthesized at high temperature, during thermal oxidation the formation of oxygen vacancies in TiO_2 was expected, which created Ti^{3+} sites. The Ti^{3+} species are also responsible for visible absorption and prevention of electron-hole recombination [45], which could facilitate photocatalysis very quickly and efficiently. However, no EPR signal was observed in the case of pristine TiN NPs (Figure S12), suggesting the formation of Ti^{3+} ions took place only during the TSCT sample fabrication.

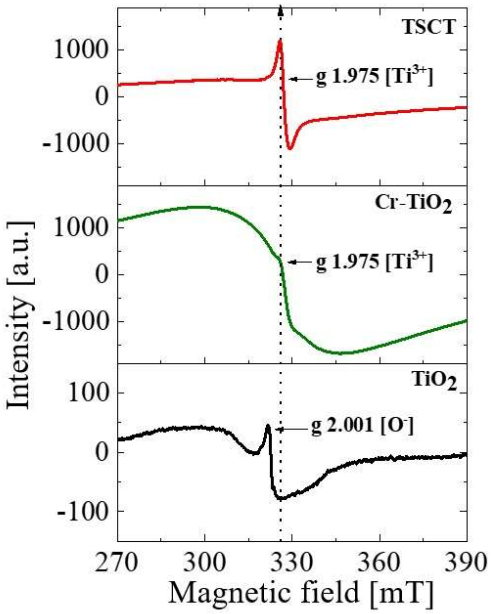

Figure 6. EPR spectra of TSCT, Cr-TiO_2 and TiO_2 samples at room temperature.

The catalytic experiments were carried out using 2 mg/mL TSCT, Cr-TiO_2 and TiO_2 NP and 10 μM MB solutions under visible light irradiation with continuous stirring. Figures 7a, 7b and 7c show the UV-VIS absorbance spectra of MB recorded at different reaction time. All the

UV-VIS measurements are done in parallel along with the dye degradation test. The strong peak at 663 nm is the characteristic peak of MB [46-47], which decreases with reaction time (highlighted with pink color in absorbance spectra). No absorbance band appears around 255 nm (highlighted with grey color in absorbance spectra) indicating no leuco form of the dye is formed during the course of the reaction [48]. No changes were observed at 663 nm after 30 days of storage.

Figure 7d shows the relative concentration of MB with time. The reduction follows pseudo-first order reaction rate kinetics (Figure 7e);

$$-\ln (C/Co) = kt,$$

where Co and C indicate initial concentration and the concentration of dyes at a reaction time t, and k is the reaction rate constant. The reaction rate constants for 2 mg/ml of TSCT, Cr-TiO_2 and TiO_2 catalyst loading were found to be 0.3, 0.09 and 0.06/min, respectively. The reaction rate changes with the catalyst loading. The k value of TSCT sample is much higher than the reported values for the other materials due to high catalyst loading. The comparison of photocatalytic degradation of MB dyes by various nanomaterials reported in the literature is shown in Table S2. For visual illustration, pictures of MB dye with TSCT sample before/after dye degradation test and picture of obtained clean water after centrifuge step are shown in Figure 7f. The blue colored MB solution becomes colorless after catalytic reaction. The high photocatalytic performance of TSCT is mainly attributed to their strong visible light absorption, large amount of paramagnetic species and large surface area, which enhances the trapping sites and interfacial charge transfer to the dye.

Further, the dye degradation performance of TSCT sample by varying the wt% (0.5 to 2 wt%) of TiN in TSCT is shown in Figure S13a. It is observed that TSCT with 1 wt% TiN is the most efficient among the three different concentrations. By increasing or decreasing the TiN NPs % in TSCT sample, the catalytic performance decreases slightly than 1wt% TiN NPs sample. This suggests that amount of TiN NPs in TSCT is crucial for efficient dye degradation. To detect the effect of sample loading in the 10 μM MB solution, 1 mg/mL and 3 mg/mL TSCT sample photocatalytic performance has been measured (Figure S13b) in addition to 2 mg/mL TSCT as shown in Figure 7. It is observed that MB degradation occur faster with increasing the loading amount of TSCT photocatalyst. For higher catalyst loading, the MB degradation occur faster as the availability of active sites increases. Furthermore, the MB degradation performance of TSCT sample under the UV component, visible light component and full solar spectrum of the simulated solar light (AM 1.5G) is measured in Figure S13c. The TSCT shows remarkably

high dye degradation rate under the visible solar light than the UV light component and resultant dye degradation rate under the full solar spectrum also becomes very high.

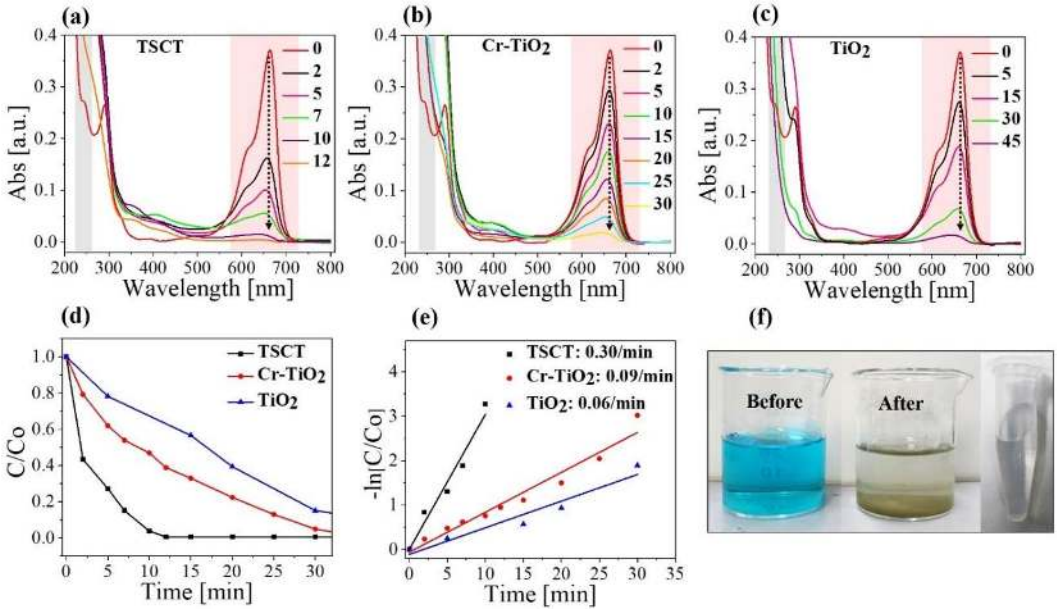

Figure 7. MB dye degradation performance with 2 mg/ml loading. Absorbance spectra of MB dye for (a) TSCT (b) Cr -TiO_2 (c) TiO_2 NPs. The pink and grey regions in the absorbance spectra represent the absorbance region for MB and leuco methylene blue, respectively. (d) Relative concentration as a function of time (e) The relative concentration is fitted to a Pseudo-first-order reaction rate equation, inset shows the rate constant values (f) Photos of before/after MB dye degradation by TSCT and water obtained after centrifuge.

Similar to the measurements for the powder samples, the photocatalytic dye degradation performances for P-Marimos loaded with the three NPs were investigated. The pictures of P-Marimo without and with each NPs are presented in Figure S14. The absorbance spectra of MB dye with TSCT-loaded P-Marimo shows 99% dye degradation within 15 minutes which is much faster than the Cr-TiO_2–loaded P-Marimo and TiO_2 –loaded ones as shown in Figure S15a, 15b and 15c. No absorption band is found at around 255 nm (highlighted with grey color in absorbance spectra) indicating absence of leuco methylene blue formation in reaction. The relative concentration with time is shown in Figure 8a and the fitted pseudo first order reaction rate is shown in Figure 8b. The reaction rate constants of P-Marimo's with TSCT, Cr-TiO_2 and TiO_2 were found to be 0.20, 0.08 and, 0.03 /min, respectively, such that the order of rate constant becomes, TiO_2 < Cr-TiO_2< TSCT, which is same as powder samples. The pictures of before and after dye degradation by P-Marimo with TSCT along with the dye degradation

mechanism are shown in Figure 8c. The possible mechanism is that the P-Marimo initially adsorbed MB dye swiftly and then the dye degradation occurred due to the •OH and O_2•⁻ radicals generation by the immobilized photocatalyst.

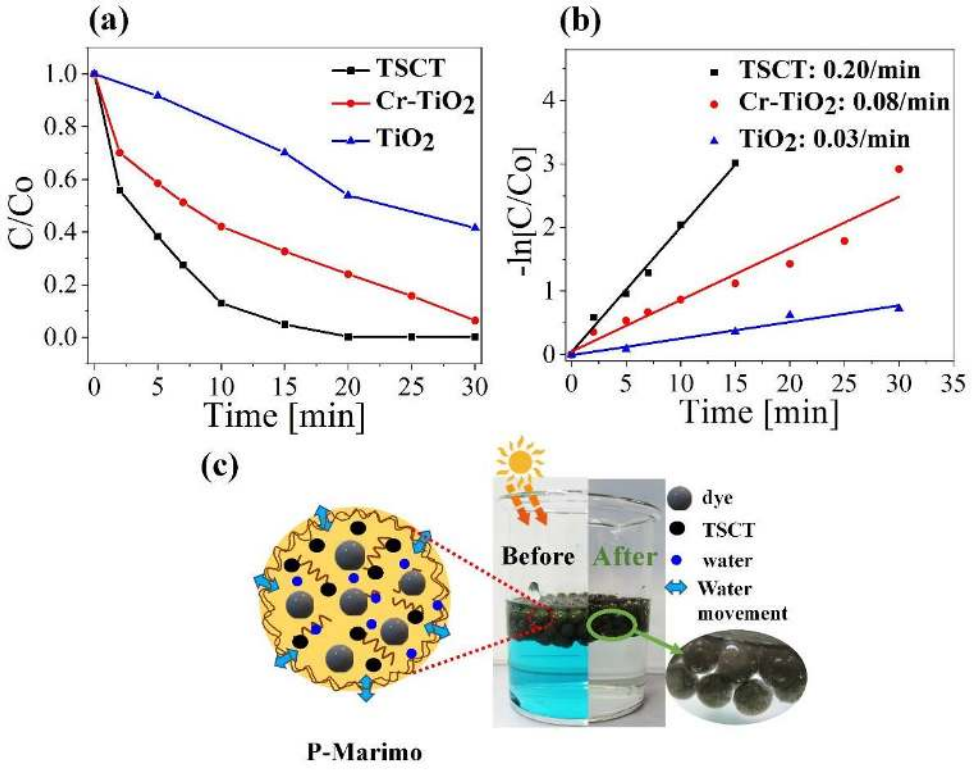

Figure 8. MB dye degradation performance of P-Marimos of TSCT, Cr-TiO_2 and TiO_2 (a) The relative concentration as a function of time. (b) The relative concentration is fitted to a Pseudo-first-order reaction rate equation, inset shows the rate constant values. (c) Schematic of dye degradation by P-Marimos and photos of before and after dye degradation by TSCT P-Marimos.

As shown in Figures 7d and 8a, the 99% degradation of MB were achieved within 10 and 15 minutes by TSCT and their P-Marimos, respectively. The use of suspended TSCT powder provided better results than those obtained with their respective P-Marimo structure. The slight reduction in the dye degradation efficiency was possibly due to the reduction in the area of active surface after the immobilization as well as the reduced water mobility in porous structure of Marimo beads. However, the immobilized system has the advantages over the suspended photocatalysts in terms of handling. The use of P-Marimos eliminates the post-process filtration

step to remove the powder photocatalyst from treated water. It opens up a facile approach to recycle the powder catalysts with eco-friendly alginate.

Photoactivity retention in the dark: As a next step, the retention of the photocatalytic activity in the dark for TSCT sample has been observed, however, this effect has not observed for bare Cr-TiO_2 and TiO_2. The MB dye degradation in the dark has been evidenced for the photocatalytic retention of TSCT and its P-Marimo as shown in Figure 9a and 9b, respectively. The TSCT in MB dye solution was firstly pre-illuminated with different exposure times under constant stirring, and stored in the dark environment for 1 hour. It is noticed that the MB dye solutions became colorless after 1 hour in dark environment. A new peak appears near 350 nm, due to the semi-reduced methylene blue radical [46, 49]. Figure 9c presents the comparison test of relative concentration of MB dye as a function of time, under light illumination but without addition of any photocatalyst (assigned as 'No photocatalyst') and with the addition of TSCT photocatalyst keeping in dark environment (assigned as 'TSCT in D'). TSCT with MB in dark shows slight decrease in concentration of MB and then saturate due to the reductive nature of TSCT. Besides, the dye degradation rates of the samples which were pre-illuminated for different time and stored in 1-hour dark environment (ascribed as TSCT in L&D, P-Marimo TSCT in L&D, Cr-TiO_2 in L&D) are shown in Figure 9c. As a representative example, the pictures of the MB dye sample with TSCT before the photocatalytic reaction, after 2-minute illumination with TSCT and subsequently 1-hour in dark are shown in Figure 9d. This confirms the TSCT sample showed retention in the photocatalytic activity in the dark environment.

The trapping and release of photogenerated electrons enable many photocatalyst to be active even after the light was turn off [50-54]. We expect similar effect in case of TSCT. The experimental observation clearly demonstrates that the degradation capability of TSCT sample in the dark was due to its large number of trapped paramagnetic species (confirmed by EPR measurement), which helped in storage of its memory of the light illumination prior to the dark environment. The production of superoxides species could be responsible for photocatalytic retention in the dark as discussed later. To further confirm the dye degradation was not due the adsorption effect, the MB dye/TSCT solution which was pre-illuminated for 2 minute and stored in the dark environment for 1 day, was heated at 50 °C for 15 min to see recovery of adsorbed MB dye. From Figure S16a, it is clear that there is no color change in MB solution after heating at 50 °C; this rule out the possibility of adsorption effect. In addition, we have re-measured the absorbance spectra of our 1-year old samples carefully stored in a dark box (these samples were pre-illuminated 2-minute and kept in dark for one year). The results of 1-year

old samples are shown in Figure S16b and S16c. For comparison, the absorbance spectra of the one year old MB solution and MB dye/Cr-TiO_2 solution are also shown in Figure S16b. It is clear that there are no change in color or absorbance after one year of storage, this confirms that TSCT completely degraded the dyes.

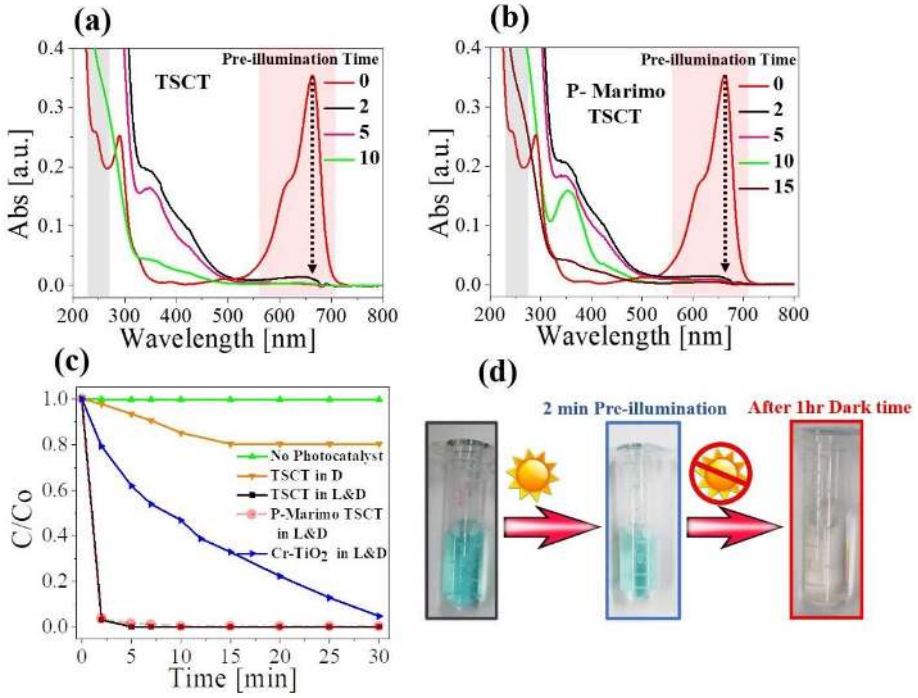

Figure 9. MB degradation performance pre-illuminated for various times and after being stored in the dark environment; (a) TSCT performance, and (b) P-Marimo TSCT performance. The pink and grey regions in absorbance spectra representsthe absorbance region for MB and leuco methylene blue, respectively. (c) MB dye degradation rate comparison for TSCT, P-Marimo TSCT and Cr-TiO_2 under different pre-illuminations time and then in the 1-hour dark. In the legend, 'L' and 'D' represent light and dark, respectively. (d) Images of dye degradation sample by TSCT, just after 2 minute pre-illumination and same sample after keeping 1 hour in dark.

To further study the catalytic activity of the TSCT, its photocatalytic degradation effect on methyl orange (MO) dye was also examined under light illumination and in dark environment as shown in the Figure S17. Figure 10 shows the comparison test of MO dye degradation rate, without an addition of any photocatalyst in the presence of light (assigned as 'No photocatalyst') and with TSCT in dark environment (assigned as 'TSCT in D'). A slight degradation has been observed without any light-illumination. The MO dye degradations were also observed for the TSCT under light illumination (assigned as 'TSCT in L') and the TSCT

pre-illuminated for 1 to 15 minute and kept in dark for one hour (assigned as 'TSCT in L&D). Figure S17 shows the MO absorbance for 'TSCT in L' and pre-illumination time dependence for 'TSCT in L&D'. The MO dye-containing solution becomes colorless after 5 minutes pre-illumination and stored in dark environment for 1 hour as shown in Figure 10b. These results clearly demonstrate the high degradation efficiency of TSCT for MO degradation and retention of its photocatalytic activity even in dark.

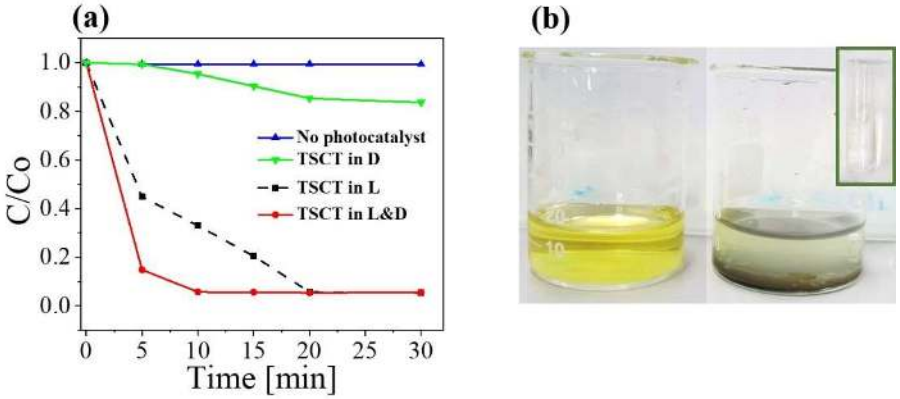

Figure 10. (a) MO dye degradation rate compared for TSCT in light and dark. 'L' and 'D' in the legend represent light and dark, respectively. (b) Optical images of dye degradation by TSCT where the dye solution was pre-illuminated for 5 minutes and kept in dark for one hour. Inset image shows the clear water after centrifuge.

In order to detect •OH and O_2•$^-$ radicals in this reaction, the effect of radical scavengers on the degradation process was examined. We used 2 mg/ml TSCT in 10 µM MB in the various solvent such as methanol (99.8%), N_2 purged (2h) H_2O and 5 mM silver nitrate ($AgNO_3$) as shown in Figure 11a. When •OH radical scavengers methanol was used as reaction medium, the MB degradation rate decreased because of the formation of •OH radicals [55]. The addition of $AgNO_3$ as electron scavenger significantly decreases the MB degradation in comparison to H_2O with no scavenger [56-57]. This suggests that $AgNO_3$ prevented the reaction of electrons with dye/O_2 molecules and decreased the degradation rate. In addition, N_2 was purged to perform MB degradation test in oxygen free atmosphere. The reaction rate of MB degradation decreased compared to air-equilibrated conditions. In the presence of dissolved O_2, the MB degradation rate was higher indicating the role of dissolve oxygen in the degradation of dyes. These results prove that the transfer of electron to MB and reaction with dissolved oxygen or water by forming •OH, as well as O_2•$^-$ which further generates •OH for the dye degradation process.

To provide further proof of the presence of •OH and O_2•$^-$, the 5, 5-Dimethyl-1-pyrroline N-oxide (DMPO) spin-trap EPR spectroscopy measurement was employed (Figure 11b). Due to difficulty in detection of •OH and O_2•$^-$ directly in EPR measurements due to their high reactivities and short lifetimes, DMPO is often used as • OH or O_2•$^-$ traps to form relatively stable species (DMPO−OH adduct) [58]. In a 100 µL aqueous solution of TSCT NPs with the addition of 10 µL of DMPO was added and the EPR spectrum was recorded. The EPR spectrum of the DMPO is presented in Figure 11b. The EPR spectrum of aqueous TSCT suspension in the DMPO shows the characteristic signal of the DMPO−OH adduct [55], because DMPO captured the •OH and O_2•$^-$ radicals to produce in the solution and formed a DMPO−OH adduct which shows an EPR signal.

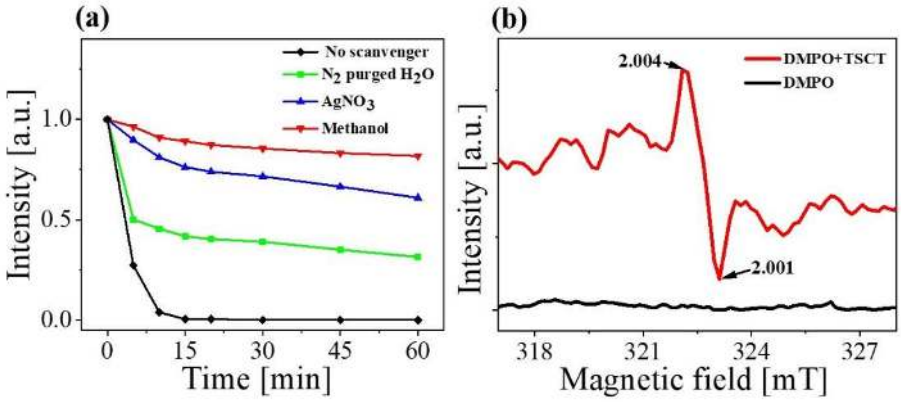

Figure 11. (a) Effect of different radical scavenger or quencher on the degradation process of methyl orange (MB) in presence of TSCT. (b) EPR spectra of 5, 5-Dimethyl-1-pyrroline N-oxide (DMPO) and an aqueous TSCT suspension to which DMPO and ethanol have been added.

In order to obtain more information about •OH and O_2•$^-$ radicals generation by TSCT, we used 2 mg/ml TSCT in 0.5 mM TA in 2 mM NaOH and stirred. The TA acted as probe molecule which reacted with the •OH radicals and O_2•$^-$ to produce fluorescent 2-hydroxyterephthalic acid [59-60]. The PL spectra recorded after different time are shown in Figure 12. The PL intensity increased with respect to the reaction time, which clearly indicates the formation of ROS during the photocatalysis process as shown in Figure 12a.

The PL spectra were measured for 2 min pre-illuminated TA and TSCT sample and then after keeping them in dark environment for different time (Figure 12b). The PL spectra of the samples were measured and found to increase with respect to the dark environment time, depicting the production of •OH and O_2•$^-$ species in dark by TSCT. In addition, the mixture of

TA and TSCT without any pre-illumination and kept in dark environment for an hour was measured (marked as 1 hour (No pre-illumination) in Figure 12b). A weak PL intensity signal was observed from this sample. It confirms that pre-illuminated TSCT samples effectively produce radicals in the dark even after the light illumination was turned off.

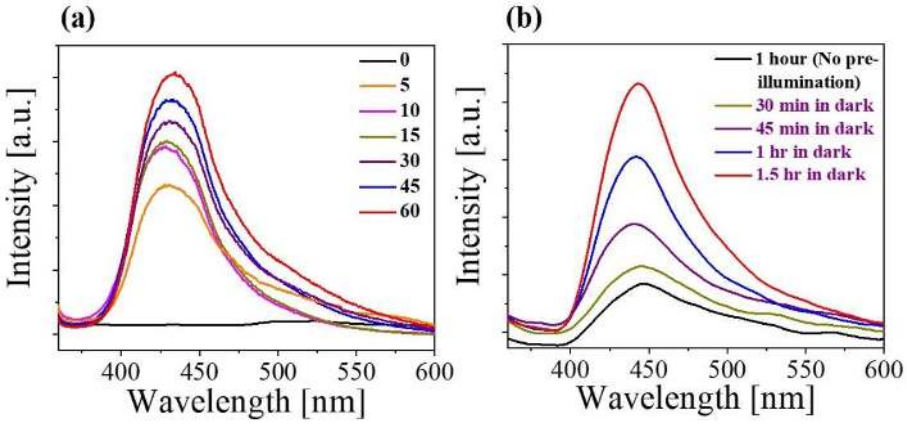

Figure 12. PL spectra of aqueous solution of terephthalic acid (TA) to detect radical generation during the photocatalytic process. (a) TSCT and TA under light illumination for different time. (b) TSCT and TA in the dark after 2-minute pre-illumination.

Apparent Quantum Yield: The photocatalytic oxidation of isopropanol (IPA) at 440 ± 15 nm was carried out to check the hydroxyl group generation by TSCT, Cr-TiO_2 and TiO_2 and to calculate the AQY [61]. The results of typical IPA photooxidation are shown in Figure S18. The Cr-TiO_2 and TiO_2 shows smaller photooxidation activity compared to TSCT under the incident light due to their lower optical absorption and low specific surface area. The significant photoactivity enhancement of TSCT could be attributed to the generated large number of hydroxyl radicals under light irradiation which oxidized IPA to acetone as per the following reaction [61],

$$CH_3CHOHCH_3 + e^- + O_2 + H^+ \rightarrow CH_3COCH_3 + \bullet OH + H_2O,$$

or,

$$CH_3CHOHCH_3 + \bullet OH + (h^+ + OH^-) \rightarrow CH_3COCH_3 + H_2O + H^+ + e^-.$$

The calculated apparent quantum yields (AQYs) at 440 ± 15 nm for TSCT, Cr-TiO_2 and TiO_2 are 36%, 15%, and 0.2%, respectively. The AQY was calculated by the following equation,

$$\text{AQY} = \frac{\text{No.of generated acetone}}{\text{No.of incident photons}} \times 100\%$$

The AQY results quantitatively reveal that TSCT has the highest photocatalytic activity among the three samples.

Photocatalytic activity of TSCT: To understand the dye degradation mechanism of the TSCT nanocomposite, Figure 13 shows an example of a schematic and energy band diagram of proposed possible mechanism under solar illumination as well as in dark. The standard redox potentials of dyes with respect to vacuum energy level and normal hydrogen electrode (NHE) scale of different reactive species are shown in Figure 13a and S19. TiN forms heterojunction with Cr-TiO_2 NPs which improves the separation of photogenerated electron–hole pairs due to the Fermi energy differences between TiN and Cr-TiO_2 NPs. Using Kelvin force probe microscope, the work functions of TiN and Cr-TiO_2 were measured to be ~ 4.5 eV [62-63], and ~ 6.0±0.5 eV, respectively, and from the literature the electron affinity of the TiO_2 is 4.2 eV [64-65]. When TSCT was illuminated with solar light, the TiN exhibited plasmonic behavior above 567 nm to have strong single-particle electronic excitation ~~below it~~. The TiN helped to increase the solar light absorption of the entire system and generated hot carriers to enhance the catalytic reaction. Therefore, when TSCT sample was irradiated by sunlight, holes were expected to be injected from TiN to Cr-TiO_2 (Figure 13b) [20-21, 66]. Although TiN NPs were coated with ~ 2 nm thick SiO_2 layer, it is possible for photoexcited carriers to tunnel through the SiO_2 layer, generating superoxides species for degradation of organic dyes [52, 67-68]. Additionally, the TiN in TSCT photocatalyst contributed to increase the electrical conductivity.

Another pathway is that the electron storage in TiN NPs shifted the apparent Fermi level of the Cr-TiO_2/TiN composite to be more negative, and this in turn made the TSCT more reductive. This reductive nature of the TSCT supplied electrons even in dark conditions, which dissipated across the surface resulting in the formation of ROS that was also confirmed from the TSCT and TA reaction study (Figure 12). Under light and in dark, the CB electrons as well as Ti^{3+} ions could reduce surface-adsorbed oxygen on active sites of photocatalyst NPs to form $O_2^{\bullet-}$ [44, 69]. Moreover, the reaction of valence band holes with surface adsorbed H_2O resulted in the formation of •OH radicals instead of combining with electrons due to their strong oxidizing ability [70]. The subsequent release of the electrons/holes in the dark may have triggered the following reactions with oxygen and water:

$$O_2 + e^- \rightarrow O_2^{\bullet-}$$

$$O_2^{\bullet-} + 2H^+ \rightarrow \bullet 2OH.$$

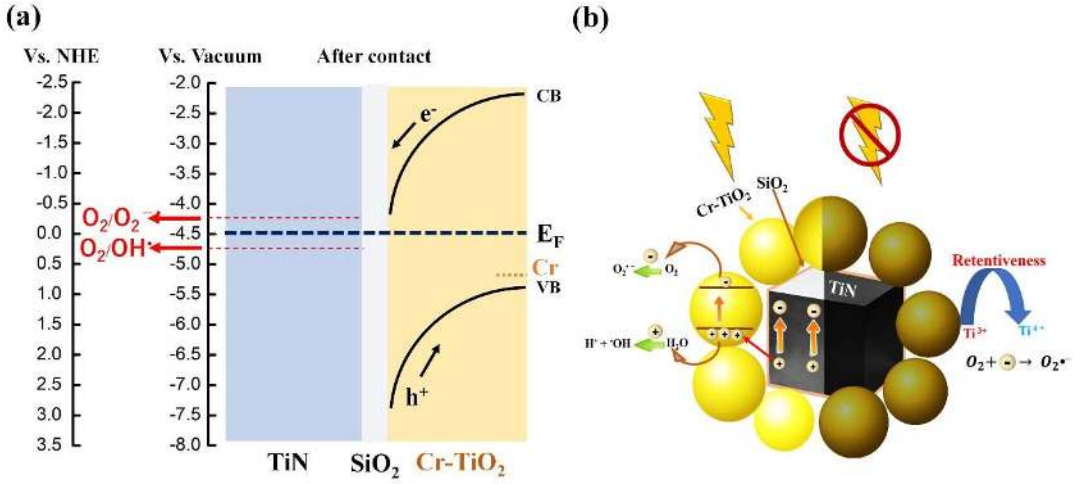

Figure 13. (a) A possible energy level diagram of TSCT and standard redox potential of different oxidative species with respect to vacuum energy levels and NHE. (b) A schematic illustration of the TSCT heterojunction and a possible photoinduced catalytic mechanism under light illumination and in dark.

Finally, recyclability and stability of P-Marimo are studied. It was found that the degradation rate of the P-Marimo remained unchanged after 10 times of repeated use. The recyclability test clearly shows that TCSC P-Marimo were highly reusable (Figure S20). To examine the stability of the P-Marimo in dye-containing water, its diameter was measured before and after each degradation/decomposition cycle. The P-Marimo diameter remained the same in all the experiments even after 25 cycles of water-purifications. This demonstration refines that the amount of calcium present in the beads was enough to make the inter-chain associations firmly sustained during the recycling. The long-lasting catalytic activity, even in dark, readiness in the recyclability as well as facile separation of catalysts from the purified water, are certainly advantageous for practical applications.

4. Conclusion

In summary, we have demonstrated the degradation of dyes by NPs and Marimo structure of TSCT under sunlight as well as in dark. Our experimental results indicated that TSCT can degrade the dyes by transferring electrons from Cr-TiO_2 to the dye molecules or by creating superoxide and hydroxyl radical with and without irradiating visible light. The catalytic activity of TSCT was several times higher than the biphasic and anatase Cr-TiO_2. By embedding TSCT powder into the gel structure of P-Marimo beads, easy handling and multiple uses of TSCT catalysts were realized while keeping their catalytic activity nearly the same. Overall, highly

efficient and long-lasting catalytic performance of P-Marimo TSCT under sunlight as well as in dark will provide a simple, environment-friendly, and cost-effective industrial treatment method for contaminated water.

ASSOCIATED CONTENT

Supporting Information. Optical pictures of different samples; Schematic representation of synthesis steps of SiO_2 layer onto TiN NPs; SEM images of TiO_2, Cr-TiO_2, TSCT and TiN; XRD plot of B-Cr-TiO_2 NPs, TiN NPs and TSCT; Raman spectra of TiN and B-Cr-TiO_2; Nitrogen adsorption desorption isotherm of TSCT, TiN, TiO_2, Cr-TiO_2 and B-Cr-TiO_2; TEM and HRTEM images of B-Cr-TiO_2; XPS of TSCT; EPR spectrum of TiN NPs; MB dye degradation performance of P-Marimo; absorbance spectra of MB for TSCT, Cr-TiO_2, TiO_2; Pictures of synthesized P-Marimos: without any NPs loading and with TiO_2, Cr-TiO_2 and TSCT; MB dye degradation rate of TSCT with different ratio of TiN NPs in TSCT hybrid structure and MB conc. as a function of catalyst loading; MO dye degradation by TSCT in the light and dark environment; Photoactivity comparison of typical IPA oxidation by TSCT, Cr-TiO_2 and TiO_2; Schematic of energy band diagram of TSCT before contact with respect to vacuum and NHE levels; Degradation efficiency of MB (10 μM) by TSCT P-Marimo in successive cycles of uses; Table of crystallite size and BET surface area of TiO_2, Cr -TiO_2, B-Cr-TiO_2, TiN and TSCT samples; Comparison of photocatalytic degradation of MB dyes by various nanomaterials reported in the literature.

AUTHOR INFORMATION

Corresponding Author

SHINDE.Satishlaxman@nims.go.jp (Satish Laxman Shinde)
sishii@nims.go.jp (Satoshi Ishii)
NAGAO.Tadaaki@nims.go.jp (Tadaaki Nagao)

Author Contributions

[†]M. Kaur and S. L. Shinde contributed equally. The manuscript was written through contributions of all authors. All authors have given approval to the final version of the manuscript.

Funding Sources

This work is partially supported by JSPS KAKENHI. T. Nagao, S. L. Shinde and S. Ishii received funding from JSPS KAKENHI (16H06364, 16K17496, and 17H04801), T. Nagao received funding from CREST "Phase Interface Science for Highly Efficient Energy Utilization" (JPMJCR13C3), Japan Science and Technology Agency, Japan Prize Foundation, and the Japan Association for Chemical Innovation.

ORCID

Satish Laxman Shinde: 0000-0002-0353-3705

Satoshi Ishii: 0000-0003-0731-8428

Tadaaki Nagao: 0000-0002-6746-2686

ACKNOWLEDGMENT

We would like to thank Dr. Lok Kumar Shrestha (NIMS) for the BET measurements.

ABBREVIATIONS

TSCT, TiN/SiO_2/Cr-TiO_2; TiN, titanium nitride; P-Marimo, 3D photocatalytic balls; ROS, reactive oxygen species; B-Cr-TiO_2, biphasic Cr-TiO_2.

REFERENCES

1. Jardim, W.; Moraes, S.; Takiyama, M., Photocatalytic degradation of aromatic chlorinated compounds using TiO_2: toxicity of intermediates. *Water Res.* **1997,** *31* (7), 1728-1732.
2. Konstantinou, I. K.; Albanis, T. A., TiO_2-assisted photocatalytic degradation of azo dyes in aqueous solution: kinetic and mechanistic investigations: a review. *Appl. Catal. B-Environ.* **2004,** *49* (1), 1-14.
3. Dalton, J. S.; Janes, P. A.; Jones, N.; Nicholson, J. A.; Hallam, K. R.; Allen, G. C., Photocatalytic oxidation of NO_x gases using TiO_2: a surface spectroscopic approach. *Environ. Pollut.* **2002,** *120* (2), 415-422.
4. Bahnemann, D., Photocatalytic water treatment: solar energy applications. *Sol. Energy* **2004,** *77* (5), 445-459.
5. Elmolla, E. S.; Chaudhuri, M., Photocatalytic degradation of amoxicillin, ampicillin and cloxacillin antibiotics in aqueous solution using UV/TiO_2 and UV/H_2O_2/TiO_2 photocatalysis. *Desalination* **2010,** *252* (1-3), 46-52.
6. Ishii, S.; Sugavaneshwar, R. P.; Nagao, T., Titanium nitride nanoparticles as plasmonic solar heat transducers. *J. Phys. Chem. C* **2016,** *120* (4), 2343-2348.
7. Hirakawa, T.; Yawata, K.; Nosaka, Y., Photocatalytic reactivity for O^{2-} and OH radical formation in anatase and rutile TiO_2 suspension as the effect of H_2O_2 addition. *Appl. Catal. A-Gen.* **2007,** *325* (1), 105-111.

8. Sun, L.; Bolton, J. R., Determination of the quantum yield for the photochemical generation of hydroxyl radicals in TiO_2 suspensions. *J. Phys. Chem.* **1996,** *100* (10), 4127-4134.
9. Fujishima, A.; Honda, K., Electrochemical photolysis of water at a semiconductor electrode. *nature* **1972,** *238* (5358), 37-38.
10. Tian, B.; Li, C.; Zhang, J., One-step preparation, characterization and visible-light photocatalytic activity of Cr-doped TiO_2 with anatase and rutile bicrystalline phases. *Chem. Eng. J.* **2012,** *191*, 402-409.
11. Di Paola, A.; Bellardita, M.; Ceccato, R.; Palmisano, L.; Parrino, F., Highly active photocatalytic TiO_2 powders obtained by thermohydrolysis of $TiCl_4$ in water. *J. Phys. Chem.* **2009,** *113* (34), 15166-15174.
12. Anpo, M.; Ichihashi, Y.; Takeuchi, M.; Yamashita, H., Design of unique titanium oxide photocatalysts by an advanced metal ion-implantation method and photocatalytic reactions under visible light irradiation. *Res. Chem. Intermediat.* **1998,** *24* (2), 143-149.
13. Zhu, J.; Deng, Z.; Chen, F.; Zhang, J.; Chen, H.; Anpo, M.; Huang, J.; Zhang, L., Hydrothermal doping method for preparation of Cr^{3+}-TiO_2 photocatalysts with concentration gradient distribution of Cr^{3+}. *Appl. Catal. B: Environ.* **2006,** *62* (3-4), 329-335.
14. Fan, X.; Chen, X.; Zhu, S.; Li, Z.; Yu, T.; Ye, J.; Zou, Z., The structural, physical and photocatalytic properties of the mesoporous Cr-doped TiO_2. *J. Mol. Catal. A-Chem.* **2008,** *284* (1-2), 155-160.
15. Dao, T. D.; Han, G.; Arai, N.; Nabatame, T.; Wada, Y.; Hoang, C. V.; Aono, M.; Nagao, T., Plasmon-mediated photocatalytic activity of wet-chemically prepared ZnO nanowire arrays. *Phys. Chem. Chem. Phys.* **2015,** *17* (11), 7395-7403.
16. Zhang, X.; Chen, Y. L.; Liu, R.S.; Tsai, D. P., Plasmonic photocatalysis. *Rep. Prog. Phys.* **2013,** *76* (4), 046401.
17. Jin, S.; Li, Y.; Xie, H.; Chen, X.; Tian, T.; Zhao, X., Highly selective photocatalytic and sensing properties of 2D-ordered dome films of nano titania and nano Ag^{2+} doped titania. *J. Mater. Chem.* **2012,** *22* (4), 1469-1476.
18. Hou, W.; Cronin, S. B., A review of surface plasmon resonance-enhanced photocatalysis. *Adv. Funct. Mater.* **2013,** *23* (13), 1612-1619.
19. Ishii, S.; Shinde, S. L.; Jevasuwan, W.; Fukata, N.; Nagao, T., Hot electron excitation from titanium nitride using visible light. *ACS Photonics* **2016,** *3* (9), 1552-1557.
20. Li, C.; Yang, W.; Liu, L.; Sun, W.; Li, Q., In situ growth of TiO_2 on TiN nanoparticles for non-noble-metal plasmonic photocatalysis. *RSC Adv.* **2016,** *6* (76), 72659-72669.
21. Naldoni, A.; Guler, U.; Wang, Z.; Marelli, M.; Malara, F.; Meng, X.; Besteiro, L. V.; Govorov, A. O.; Kildishev, A. V.; Boltasseva, A.; Shalaev, V. M., Broadband Hot-Electron Collection for Solar Water Splitting with Plasmonic Titanium Nitride. *Adv. Opt. Mater.* **2017,** *5* (15), 1601031.
22. Yoo, B.; Kim, K.J.; Kim, Y. H.; Kim, K.; Ko, M. J.; Kim, W. M.; Park, N.G., Titanium nitride thin film as a novel charge collector in TCO-less dye-sensitized solar cell. *J. Mater. Chem.* **2011,** *21* (9), 3077-3084; Fakhouri, H.; Arefi-Khonsari, F.; Jaiswal, A.; Pulpytel, J., Enhanced visible light photoactivity and charge separation in TiO_2/TiN bilayer thin films. *Appl. Catal. A-Gen.* **2015,** *492*, 83-92.
23. Ishii, S.; Shinde, S. L.; Nagao, T., Nonmetallic Materials for Plasmonic Hot Carrier Excitation. *Adv. Opt. Mater.*, **2019**, *7* (1), 1800603-1800615
24. Scotti, R.; D'Arienzo, M.; Morazzoni, F.; Bellobono, I. R., Immobilization of hydrothermally produced TiO_2 with different phase composition for photocatalytic degradation of phenol. *Appl. Catal. B-Environ.* **2009,** *88* (3-4), 323-330.

25. McMurray, T.; Byrne, J.; Dunlop, P.; Winkelman, J.; Eggins, B.; McAdams, E., Intrinsic kinetics of photocatalytic oxidation of formic and oxalic acid on immobilised TiO_2 films. *Appl. Catal. A-Gen.* **2004,** *262* (1), 105-110.
26. Nakamura, K., Synthesis of nanoparticles by thermal plasma processing and its applications. *Earozoru Kenkyu* **2014,** *29* (2), 98-103.
27. Ahmed, Y.; Yaakob, Z.; Akhtar, P., Degradation and mineralization of methylene blue using a heterogeneous photo-Fenton catalyst under visible and solar light irradiation. *Catal. Sci. Technol.* **2016,** *6* (4), 1222-1232.
28. Hussein, A. M.; Shende, R. V., Synthesis of Visible-light Activated Nanoparticles for H_2 Production.*Tech Connect World Innovation Conference and Expo, Nanotech.* **2014**, Washington, DC.
29. Subha, P.; Jayaraj, M., Solar photocatalytic degradation of methyl orange dye using TiO_2 nanoparticles synthesised by sol–gel method in neutral medium. *J. Exp. Nanosci.* **2015,** *10* (14), 1106-1115.
30. Mendiola-Alvarez, S. Y.; Guzmán-Mar, J. L.; Turnes-Palomino, G.; Maya-Alejandro, F.; Caballero-Quintero, A.; Hernández-Ramírez, A.; Hinojosa-Reyes, L., Synthesis of Cr^{3+}-doped TiO_2 nanoparticles: characterization and evaluation of their visible photocatalytic performance and stability. *Environ. Technol.* **2017**, 1-10.
31. Ohsaka, T.; Izumi, F.; Fujiki, Y., Raman spectrum of anatase, TiO_2. *J. Raman Spectrosc.* **1978,** *7* (6), 321-324.
32. Pedraza-Avella, J.; López, R.; Martinez-Ortega, F.; Páez-Mozo, E.; Gómez, R. In *Effect of chromium doping on visible light absorption of nanosized titania sol-gel*, *J. Nano Res., Trans Tech Publ:* 2009; pp 95-104.
33. Choudhury, B.; Choudhury, A., Structural, optical and ferromagnetic properties of Cr doped TiO_2 nanoparticles. *Mater. Sci. Eng. B* **2013,** *178* (11), 794-800.
34. Subramanian, B.; Jayachandran, M., Characterization of reactive magnetron sputtered nanocrystalline titanium nitride (TiN) thin films with brush plated Ni interlayer. *J. Appl. Electrochem.* **2007,** *37* (9), 1069-1075.
35. Ponon, N. K.; Appleby, D. J.; Arac, E.; King, P.; Ganti, S.; Kwa, K. S.; O'Neill, A., Effect of deposition conditions and post deposition anneal on reactively sputtered titanium nitride thin films. *Thin Solid Films* **2015,** *578*, 31-37.
36. Wang, W. K.; Chen, J. J.; Zhang, X.; Huang, Y. X.; Li, W. W.; Yu, H. Q., Self-induced synthesis of phase-junction TiO_2 with a tailored rutile to anatase ratio below phase transition temperature. *Sci. Rep.* **2016,** *6*, 20491.
37. Chimupala, Y.; Junploy, P.; Hardcastle, T.; Westwood, A.; Scott, A.; Johnson, B.; Brydson, R., Universal synthesis method for mixed phase TiO_2 (B)/anatase TiO_2 thin films on substrates via a modified low pressure chemical vapour deposition (LPCVD) route. *J. Mater. Chem. A* **2016,** *4* (15), 5685-5699.
38. Saha, N. C.; Tompkins, H. G., Titanium nitride oxidation chemistry: An x-ray photoelectron spectroscopy study. *J. Appl. Phys.* **1992,** *72* (7), 3072-3079.
39. Panda, P.; Ramaseshan, R.; Sahoo, M.; Krishna, N. G.; Yadav, A.; Jha, S.; Bhattacharyya, D., Local crystal structure in the vicinity of Cr in doped AlN thin films studied by X-ray absorption spectroscopy. *Phys. Chem. Chem. Phys.* **2018,** *20* (18), 13084-13091.
40. Barbagiovanni, E.; Goncharova, L.; Simpson, P., Electronic structure study of ion-implanted Si quantum dots in a SiO_2 matrix: analysis of quantum confinement theories. *Phys. Rev. B* **2011,** *83* (3), 035112.
41. Murray, W. A.; Barnes, W. L., Plasmonic materials. *Adv. Mater.* **2007,** *19* (22), 3771-3782.

42. Shiraishi, Y.; Tsukamoto, D.; Sugano, Y.; Shiro, A.; Ichikawa, S.; Tanaka, S.; Hirai, T., Platinum nanoparticles supported on anatase titanium dioxide as highly active catalysts for aerobic oxidation under visible light irradiation. *ACS Catal.* **2012,** *2* (9), 1984-1992.
43. Reyes-Garcia, E. A.; Sun, Y.; Reyes-Gil, K. R.; Raftery, D., Solid-state NMR and EPR analysis of carbon-doped titanium dioxide photocatalysts. *Solid State Nucl. Magn.* **2009,** *35* (2), 74-81.
44. Yang, G.; Jiang, Z.; Shi, H.; Xiao, T.; Yan, Z., Preparation of highly visible-light active N-doped TiO_2 photocatalyst. *J. Mater. Chem.* **2010,** *20* (25), 5301-5309.
45. Xiong, L. B.; Li, J. L.; Yang, B.; Yu, Y., Ti^{3+} in the surface of titanium dioxide: generation, properties and photocatalytic application. *J. Nanomater.* **2012,** *2012*.
46. Galagan, Y.; Su, W.F., Reversible photoreduction of methylene blue in acrylate media containing benzyl dimethyl ketal. *J. Photoch. Photobio. A.* **2008,** *195* (2-3), 378-383.
47. Sohrabnezhad, S., Study of catalytic reduction and photodegradation of methylene blue by heterogeneous catalyst. *Spectrochim. Acta A Mol. Biomol. Spectrosc.* **2011,** *81* (1), 228-235.
48. Impert, O.; Katafias, A.; Kita, P.; Mills, A.; Pietkiewicz-Graczyk, A.; Wrzeszcz, G., Kinetics and mechanism of a fast leuco-Methylene Blue oxidation by copper (II)–halide species in acidic aqueous media. *Dalton Trans.* **2003,** (3), 348-353.
49. Muthyala, R., Chemistry and applications of leuco dyes. *Springer Science & Business Media:* **2006**.
50. Wolanov, Y.; Prikhodchenko, P. V.; Medvedev, A. G.; Pedahzur, R.; Lev, O., Zinc dioxide nanoparticulates: a hydrogen peroxide source at moderate pH. *Environ. Sci. Technol.* **2013,** *47* (15), 8769-8774.
51. Rajagopalan, V., A new synergetic nanocomposite for dye degradation in dark and light. *Sci. Rep.* **2016,** *6*, 38606.
52. Cao, Y.; Gu, X.; Yu, H.; Zeng, W.; Liu, X.; Jiang, S.; Li, Y., Degradation of organic dyes by Si/SiOx core-shell nanowires: Spontaneous generation of superoxides without light irradiation. *Chemosphere* **2016,** *144*, 836-841.
53. Shinde, S. L.; Nanda, K. K., Photon-free Degradation of Dyes by Ge/GeO_2 Porous Microstructures. *ACS Sust. Chem. Eng.* **2019,** 7, 6611-6618.
54. Liu, L.; Sun, W.; Yang, W.; Li, Q.; Shang, J. K., Post-illumination activity of SnO_2 nanoparticle-decorated Cu_2O nanocubes by H_2O_2 production in dark from photocatalytic "memory". *Sci. Rep.* **2016,** *6*, 20878.
55. Gu, L.; Wang, J.; Cheng, H.; Zhao, Y.; Liu, L.; Han, X., One-step preparation of graphene-supported anatase TiO2 with exposed {001} facets and mechanism of enhanced photocatalytic properties. *ACS Appl. Mater. Interfaces* **2013,** *5* (8), 3085-3093.
56. Chen, Z.; Zhang, N.; Xu, Y. J., Synthesis of graphene–ZnO nanorod nanocomposites with improved photoactivity and anti-photocorrosion. *Cryst. Eng. Comm.* **2013,** *15* (15), 3022-3030.
57. Zhang, Y.; Zhang, N.; Tang, Z. R.; Xu, Y. J., Graphene transforms wide band gap ZnS to a visible light photocatalyst. The new role of graphene as a macromolecular photosensitizer. *ACS nano* **2012,** *6* (11), 9777-9789.
58. Kochany, J.; Bolton, J. R., Mechanism of photodegradation of aqueous organic pollutants. 1. EPR spin-trapping technique for the determination of hydroxyl radical rate constants in the photooxidation of chlorophenols following the photolysis of hydrogen peroxide. *J. Phys. Chem.* **1991,** *95* (13), 5116-5120.
59. Wu, L.; Xing, J.; Hou, Y.; Xiao, F. Y.; Li, Z.; Yang, H. G., Fabrication of regular ZnO/TiO2 heterojunctions with enhanced photocatalytic properties. *Chem-Eur J.* **2013,** *19* (26), 8393-8396.

60. Wang, Z. J.; Garth, K.; Ghasimi, S.; Landfester, K.; Zhang, K. A., Conjugated Microporous Poly(Benzochalcogenadiazole)s for Photocatalytic Oxidative Coupling of Amines under Visible Light. *Chem. Sus. Chem.* **2015,** *8* (20), 3459-3464.
61. Li, Y.; Ouyang, S.; Xu, H.; Wang, X.; Bi, Y.; Zhang, Y.; Ye, J., Constructing solid–gas-interfacial fenton reaction over alkalinized-C_3N_4 photocatalyst to achieve apparent quantum yield of 49% at 420 nm. *J. Am. Chem. Soc.* **2016,** *138* (40), 13289-13297.
62. Didden, A.; Battjes, H.; Machunze, R.; Dam, B.; van de Krol, R., Titanium nitride: A new Ohmic contact material for n-type CdS. *J. Appl. Phys.* **2011,** *110* (3), 033717.
63. Shinde, S. L.; Ishii, S.; Dao, T. D.; Sugavaneshwar, R. P.; Takei, T.; Nanda, K. K.; Nagao, T., Enhanced solar light absorption and photoelectrochemical conversion using TiN nanoparticle-incorporated C_3N_4–C dot sheets. *ACS Appl. Mater. Interfaces* **2018,** *10* (3), 2460-2468.
64. Subrahmanyam, A.; Biju, K.; Rajesh, P.; Kumar, K. J.; Kiran, M. R., Surface modification of sol gel TiO_2 surface with sputtered metallic silver for Sun light photocatalytic activity: initial studies. *Sol. Energy Mater. Sol. Cells* **2012,** *101*, 241-248.
65. Pfeifer, V.; Erhart, P.; Li, S.; Rachut, K.; Morasch, J.; Brötz, J.; Reckers, P.; Mayer, T.; Rühle, S.; Zaban, A., Energy band alignment between anatase and rutile TiO_2. *J. Phys. Chem. Lett.* **2013,** *4* (23), 4182-4187.
66. Fakhouri, H.; Arefi-Khonsari, F.; Jaiswal, A.; Pulpytel, J., Enhanced visible light photoactivity and charge separation in TiO_2/TiN bilayer thin films. *Appl. Catal. A-Gen.* **2015,** *492*, 83-92.
67. Fischetti, M. V.; DiMaria, D. J.; Dori, L.; Batey, J.; Tierney, E.; Stasiak, J., Ballistic electron transport in thin silicon dioxide films. *Phys. Rev. B* **1987,** *35* (9), 4404-4415.
68. Matsuo, N.; Miura, T.; Urakami, A.; Miyoshi, T., Analysis of direct tunneling for thin SiO2 film. *Jpn. J. Appl. Phys.* **1999,** *38* (7R), 3967.
69. Wang, J.; Li, H.; Li, H.; Zou, C., Mesoporous TiO_2− xAy (A= N, S) as a visible-light-response photocatalyst. *Solid State Sci.* **2010,** *12* (4), 490-497.
70. Etacheri, V.; Di Valentin, C.; Schneider, J.; Bahnemann, D.; Pillai, S. C., Visible-light activation of TiO_2 photocatalysts: Advances in theory and experiments. *J. Photochem. Photobio. C-Photochem. Rev.* **2015,** *25*, 1-29.

Table of Contents

P-Marimo